Exp Fluids (2014) 55:1651
DOI 10.1007/s00348-013-1651-y

RESEARCH ARTICLE

A novel approach for the isolation of the sound and pseudo-sound contributions from near-field pressure fluctuation measurements: analysis of the hydroacoustic and hydrodynamic perturbation in a propeller-rudder system

Mario Felli · Silvano Grizzi · Massimo Falchi

Received: 27 May 2013 / Revised: 6 December 2013 / Accepted: 13 December 2013

Abstract The main scope of the present work is to investigate the mechanisms underlying the hydroacoustic and hydrodynamic perturbations in a rudder operating in the wake of a free running marine propeller. The study consisted of detailed near-field pressure fluctuation measurements which were acquired on the face and back surfaces of the rudder, at different deflection angles. To this aim, a novel wavelet-filtering procedure was applied to separate and analyze distinctly the acoustic and hydrodynamic components of the recorded near-field pressure signals. The filtering procedure undertakes the separation of intermittent pressure peaks induced by the passage of eddy structures, interpreted as pseudo-sound, from homogenous background fluctuations, interpreted as sound. The use of wavelet in the filtering procedure allows to overcome the limitations of the earlier attempts based on frequency (wave number) band-pass filtering, retrieving the overall frequency content of both the acoustic and the hydrodynamic components and returning them as independent signals in the time domain. Acoustic and hydrodynamic pressure distributions were decomposed harmonically and compared to the corresponding topologies of the vorticity field, derived from earlier LDV measurements performed by Felli and Falchi (Exp Fluids 51(5):1385–1402, 2011). The study highlighted that the acoustic perturbation is mainly correlated with the unsteady load variations of the rudder and to the shear layer fluctuations of the propeller streamtube. Conversely, the dynamics of the propeller tip and hub vortices underlies the hydrodynamic perturbation.

M. Felli (✉) · S. Grizzi · M. Falchi
CNR-INSEAN, Via di Vallerano 139, 00128 Rome, Italy
e-mail: mario.felli@cnr.it

1 Introduction

Control and mitigation of noise and vibration onboard ships as well as radiated noise off-board are issues of increasing importance to the international shipbuilding industry, in view of the increasingly demanding rules and classification standards that must be complied before the ship delivery (Carlton and Vlasic 2005). As a matter of fact, in the last decade, comfort level onboard has become an important contractual item for both passenger ships and cargos, since it influences the performance and vigilance of the crew and the rating and reputation in the market (Biot and De Lorenzo 2008). On the other hand, underwater noise pollution from shipping traffic is suffering a rise estimated by 0.3–0.6 db/year since the 1960s and is a dramatic problem that has made paramount the need to mitigate and control the acoustic signature, nowadays (Hildebrand 2004).

In this scenario, the need for a major breakthrough in ship design and operation represents a target that industry and research must jointly fulfill to comply with the new standards for a safer and more sustainable shipping. In particular, research has been called to provide solutions to the twofold task to develop wide-spread and cost-effective tools to be integrated in the rapid design spiral of ships, on the one hand, and to improve the understanding of the fundamental mechanisms underlying the onboard comfort and the acoustic signature, on the other hand. In this challenge, the availability of increasingly faster and more powerful PCs as well as the assessment of advanced experimental and computational techniques has allowed to develop experimental and theoretical tools by which approaching even of the most complex mechanisms governing the hydrodynamic and hydroacoustic performance of ships. This has

Published online: 25 December 2013

widened the horizons of modern research toward complex problems of naval engineering and has allowed approaching even the most tricky and testing demands from shipyards and navies, consequently.

As a representative critical problem of naval propulsion with significant hydroacoustic and structural implications, the present paper investigates the interaction between the wake of a marine propeller and a rudder. In particular, differently from previous experimental works on this topic, which focused on the dynamics of the propeller wake structures during the interaction with the rudder (see e.g., Felli and Di Felice 2004; Felli et al. 2009; Anschau and Mach, 2009; Lücke and Streckwall 2009; Felli and Falchi 2011), attention is here given to the detailed analysis of the perturbation mechanisms behind the radiated noise and the induced vibrations in a propeller-rudder system.

In spite of the relevance of the subject due to the well-known implications for the onboard comfort and the radiated noise in naval engineering, the mechanisms underlying the generation and propagation of noise and vibrations in a propeller-rudder system is still unknown and not yet thoroughly documented in the literature. One of the reasons is that the accurate identification of the noise and vibration sources underwater is a challenging task which involves the need to analyze the acoustic and hydrodynamic pressure distributions, namely sound and pseudo-sound (Ffowcs-Williams 1992), in the near field and to possibly correlate them with the corresponding flow topologies (Howe 1960). Leaving aside the non-trivial problem to set up and perform such a state-of-the-art survey, this approach encounters the major problem in the difficulty to separate pressure signals taken in the near field into hydrodynamic and acoustic components (Tinney et al. 2007). In fact, acoustic perturbation is normally embedded into the hydrodynamic signal when pressure fluctuations are measured in the near field and this makes their separation a preparatory stage for the in-depth analysis of the underlying mechanisms of noise and vibration.

The approach introduced in the present paper undertakes near-field signals decomposition applying a wavelet-based filtering procedure in which separation of the acoustic and hydrodynamic components is addressed selecting the wavelet coefficients being, respectively, below and above a certain threshold. The time histories of the acoustic and hydrodynamic components are then retrieved by anti-transforming the two sets from the wavelet to the physical space. This procedure, inspired to the de-noising technique developed by Ruppert-Felsot et al. (2009) to quantify the intermittency of turbulent flows and recently extended to the study of the jet-noise by Grizzi and Camussi (2012), introduces two major advantages compared to the earlier attempts based on frequency (wave number) band-pass filtering methods (see e.g., Arndt et al. 1997; Guitton et al. 2007), specifically:

- filtering the wavelet coefficients preserves the temporal structure of the signal and, thus, allows to reconstruct the acoustic and hydrodynamic perturbations as independent signals in the time domain. Conversely, time information is definitively lost in Fourier-based filtering techniques since Fourier transform is able to retrieve only the global frequency content of a signal (Farge 1992). The possibility to retrieve independent acoustic and hydrodynamic signals is obviously an useful and effective feature of the wavelet-based filtering procedure;
- frequency band-pass filtering procedures do not allow for analysis of the potential acoustic and hydrodynamic perturbations across the overall frequency range of the pressure signal since they imply that all information above a specified wave number is sound and all information below is pseudo-sound (Guitton et al. 2007). This feature spoils the accuracy of the frequency band-pass filtering procedures since content of acoustic and hydrodynamic perturbations cannot be neglected at low and high frequencies, respectively, at least in the near field (Grizzi and Camussi 2012);
- unlike frequency band-pass filtering procedures in which a microphone array with several transducers is required (see e.g., Guitton et al. 2007), the method presented therein is based on the use of only two sensors. This feature makes the wavelet-based filtering procedure more practical during both the acquisition and processing stages.

In the present study, the analysis of the mechanisms underlying the generation and propagation of noise and vibrations in a propeller-rudder system was undertaken by near-field pressure fluctuation measurements performed using an array of several pressure sensors, flush mounted on the rudder surface. Any pressure fluctuation signal was, then, decomposed into its acoustic and hydrodynamic components applying the wavelet-based filtering procedure described above. Hydrodynamic and acoustic pressure fluctuation signals were analyzed separately through Fourier analysis, decomposed harmonically and correlated with phase-locked velocimetry data, measured earlier by Felli and Falchi (2011) on the rudder surface.

The paper is organized as follows. The methodologies used for pressure signal decomposition and processing are described in Sect. 2. The experimental setup, the test matrix and the test conditions are documented in Sect. 3. The analysis of the results is reported in Sect. 4. Conclusions and future works are summarized in Sect. 5.

2 Pressure signal processing techniques

2.1 Technique for the separation of the sound and pseudo-sound contributions in pressure signals

One of the main problems related to near-field pressure measurements is that only a small part of the energy associated with pressure fluctuations radiates as sound. The other pressure fluctuations does not satisfy the linear wave equation and, then, cannot be regarded as sound. This contribution, named in the literature as pseudo-sound (see Howe 1960; Ribner 1964 and Ffowcs-Williams 1992), is associated with the passage of eddy structures in the flow, and thus, it moves with a speed that is much smaller than the sonic velocity, at least for the low Mach numbers.

The main problem related to near-field noise measurements is in the difficulty to separate out the acoustic from the hydrodynamic part of pressure fluctuations (Tinney et al. 2007). In fact, these contributions are normally buried by each other in the near field of a hydrodynamic noise source where the flow field is typically dominated by the passage of turbulent structures.

This problem concerns only the near field because the passage of eddy structures is therein localized: Moving away from a noise source, the hydrodynamic contribution disappears and pressure field reduces only to sound (Howe 1960).

The problem to separate out acoustic from hydrodynamic pressure fluctuations is here overcame through the use of a proper filtering procedure, presented by Grizzi and Camussi (2012) for the study of low-Mach jet flow in air. This novel technique is here extended to a hydrodynamic application.

The methodology is based on the use of the wavelet transform (e.g., Mallat 1989; Daubechies 1992; Farge 1992) and takes inspiration from state-of-the-art filtering procedures in which wavelet was effectively used for the isolation of coherent structures from fully turbulent fluctuations (e.g., Farge 1992 and Ruppert-Felsot et al. 2009).

Such an effectiveness is the consequence of both the peculiar ability of the wavelet transform to identify intermittent events (e.g., see Chainais et al. 1999; Ruppert-Felsot et al. 2009) and the intermittent nature of the perturbation associated with the passage coherent structures (Ukeiley and Ponton 2004).

Similarly to the filtering procedures for the analysis of turbulent flows, the methodology described therein is intended to separate out the sound and pseudo-sound contributions taking advantage of the intermittent nature of the latter and the aforementioned ability of the wavelet transform to isolate intermittent events. More specifically:

- the hydrodynamic contribution (i.e., pseudo-sound), being related to the intermittent perturbation of localized coherent structures, can be assumed to compresses well into a wavelet basis, namely it could be represented by only few strong (i.e., with a large magnitude) wavelet coefficients.
- the acoustic contribution (i.e., sound) is represented by the remaining weaker coefficients of the wavelet transform which correspond to more homogeneous pressure fluctuations and, thus, which do not compress well into the wavelet basis.

Following this idea, the isolation of the hydrodynamic and acoustic contributions reduces to the selection of a proper threshold by which wavelet coefficients are separated into two sets depending on their magnitude:

- coefficients exceeding the threshold correspond to hydrodynamic pressure fluctuations or pseudo-sound;
- coefficients not exceeding the threshold correspond to acoustic pressure fluctuations or sound.

The reconstruction of the hydrodynamic and acoustic signals is then undertaken anti-transforming the two wavelet sets from the wavelet to the physical space.

From what stated above, it is evident that the accuracy of the decomposition depends strongly on the selection of the proper threshold value, which, thus, represents the most critical and tricky stage of the procedure.

The threshold level is set iteratively taking advantage of the different propagation speeds of the hydrodynamic and acoustic perturbations at low-Mach. In particular, the idea is to define an iterative procedure to estimate the propagation speeds of the hydrodynamic and acoustic perturbations from the reconstructed signals. This information is then used to properly define the threshold level that must be such to return propagation speeds of the acoustic and hydrodynamic perturbations consistent with the speed of sound and the convective speed of the flow, respectively. To this aim, the procedure requires the use of two hydrophones, namely H_1 and H_2, to calculate the delay of the cross-correlation peaks between the corresponding estimations of the hydrodynamic and acoustic signals, at each iteration. The propagation speeds of the actual acoustic and hydrodynamic perturbations are then estimated once known the distance between the two hydrophones. Hydrophones should be located in the near field, sufficiently close to each other to permit the hydrodynamic perturbation to be sensed by both transducers within a measurable time delay.

The convergence of the iteration is monitored by two criteria which must be simultaneously satisfied by the reconstructed hydrodynamic and acoustic components from the two hydrophones. One criterion is related to the

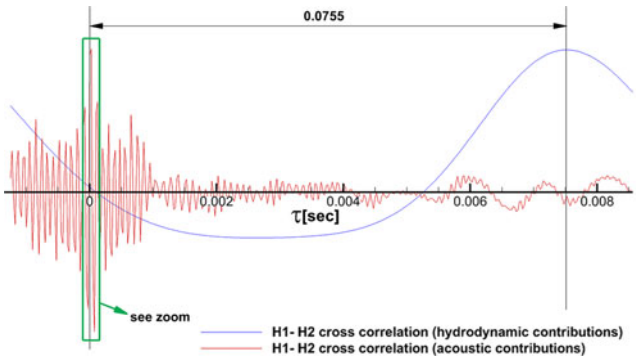

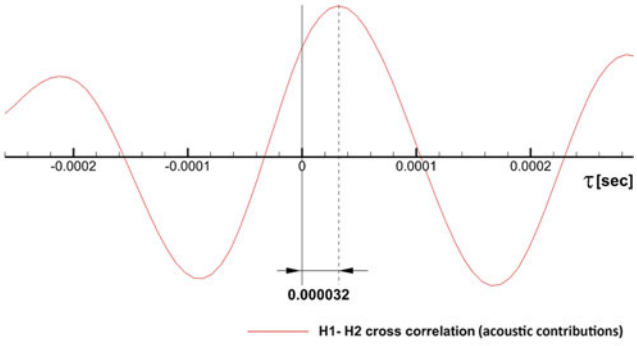

Fig. 1 Cross-correlation function of the acoustic and hydrodynamic parts between the transducers H1 and H2. Transducers H1 and H2 were 50 mm spaced. The time lags of the acoustic and hydrodynamic signals correspond to the velocities of 1,562 m/s (sound) and 6.62 m/s (pseudo-sound)

delay of the correlation peak of the hydrodynamic and acoustic signals which must correspond to a propagation velocity less than or equal to the flow velocity and greater than or equal to the ambient sound speed, respectively. The other criterion consists of the estimation of the peak ratio between the first and second cross-correlation peak in the cross-correlation function calculated between the two hydrodynamic signals, representative of the actual signal-to-noise ratio of the decomposition procedure. This ratio must be greater than a prescribed value, normally set around two (Grizzi and Camussi 2012). In fact, it is worth noting that the second correlation peak is related to a spurious contribution since it is associated with the part of the acoustic signal not yet filtered from the algorithm and still embedded in the hydrodynamic signal.

Figure 1 shows the cross-correlation functions of the two acoustic and hydrodynamic signals after the separation procedure. Cross-correlations were computed between two sensors at the distance of 50 mm.

A schematic description of the iterative process to set the proper threshold is reported hereinafter:

1. The initial level of the threshold is guessed at the first iteration applying the wavelet-based de-noising procedure described in Farge (1992), Farge et al. (1999) for the analysis of turbulent flows. A thorough description of the procedure is given in Ruppert-Felsot et al. (2009).
2. According to the selected threshold, the estimation of the hydrodynamic and acoustic contributions is obtained for the pressure fluctuations signals from hydrophones H_1 and H_2.
3. The estimated acoustic and hydrodynamic contributions from hydrophones H_1 and H_2 are cross-correlated with derive the corresponding propagation speeds and to verify the fulfillment of the convergence criteria.
4. If at least one of the convergence criteria is not satisfied, the threshold level is incremented by a discrete quantity and the process restarts from point two. The definition of the increment value of the threshold is not trivial and normally requires to analyze the trend of the signal-to-noise ratio of the decomposition procedure, for two iterations at least.

Typically, the iterative process converges after a few steps and returns two independent signals representing the time histories of the acoustic and hydrodynamic parts of pressure fluctuations.

The block diagram of Fig. 2 shows an overview of the filtering procedure.

2.2 Phase-locked harmonic analysis

Pressure signals over the rudder surface were sampled M times during one propeller revolution and then ensemble averaged according to the following relation:

$$\langle p \rangle_i = \frac{1}{N} \sum_{j=1}^{N} p_{i,j} \tag{1}$$

in which j and i are the corresponding jth revolution and the ith data point in that revolution and N the revolution number of the propeller during each acquisition.

Due to the ergodicity of the random process involved, the average pressure–time history obtained from Eq. (1) can be transposed into the frequency domain using the direct Fourier transform.Expressed in mathematical terms, Fourier's theorem asserts that for a periodic function $p(t)$ of fundamental frequency f_0, one can write $p(t)$ as the sum of basic trigonometric functions such that:

$$p(t) = \sum_{n=0}^{\infty} A_n \cos(2\pi n f_0 t + \varphi_n) \tag{2}$$

where A_n and φ_n represent amplitude and phase of the corresponding harmonic function. Equation (2) can be rearranged into:

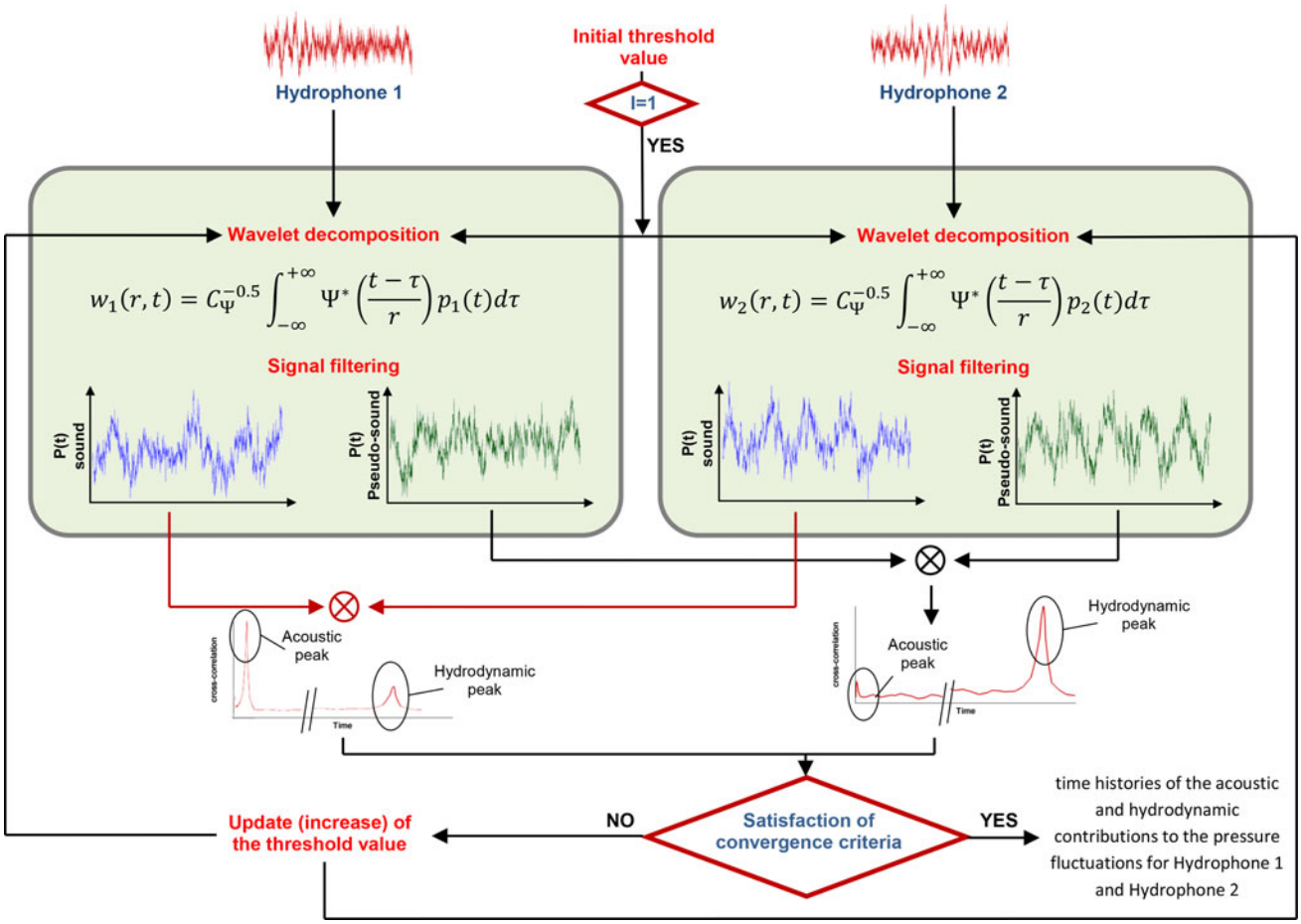

Fig. 2 Block diagram of the filtering procedure to separate out the sound and pseudo-sound contributions

$$p(t) = \sum_{n=0}^{\infty} C_n \cos(2\pi n f_0 t) + \sum_{n=0}^{\infty} S_n \sin(2\pi n f_0 t) \tag{3}$$

The determination of A_n and φ_n in (2) is now reduced to the calculation of the coefficients C_n and S_n, using the following formulas:

$$C_0 = f_0 \int_{-f_0/2}^{f_0/2} p(t)\mathrm{d}t$$

$$C_m = 2f_0 \int_{-f_0/2}^{f_0/2} p(t)\cos(2\pi m f_0 t)\mathrm{d}t \quad m \neq 0 \tag{4}$$

$$S_m = 2f_0 \int_{-f_0/2}^{f_0/2} p(t)\sin(2\pi m f_0 t)\mathrm{d}t$$

The above transform decomposes a periodically unsteady signal into its basic components, i.e., the fundamental frequency or first harmonic and its multiples or higher order harmonics, and, thus, allows sorting out the phase-locked coherent flow structures from the otherwise random unsteadiness in the flow field.

In the present work, the fundamental frequency is associated with the blade passage and corresponds to 100 Hz, the propeller rotation speed and the blade number being 25 rps and 4, respectively.

The harmonic decomposition is an extremely useful tool by which one can reconstruct the phase-locked topologies of each single harmonic in the measurements domain and isolate the corresponding perturbation sources (e.g., comparing the phase-locked representation of each harmonic to the corresponding representation of the velocity signals).

3 Experimental setup

3.1 Reference frames and dimensionless groups

Two reference systems were adopted:

- A Cartesian reference frame O–XYZ with the origin O at the intersection between the propeller disk and the

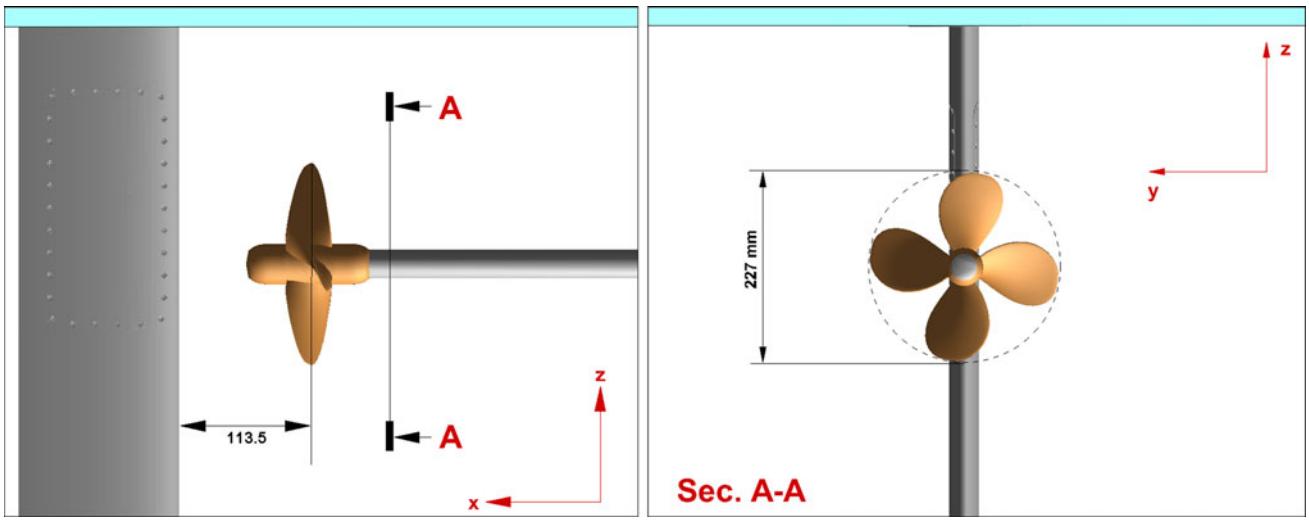

Fig. 3 Sketch of the propeller-rudder configuration

Table 1 Propeller and rudder geometrical data

Propeller blades	4
Propeller diameter	227 mm
Propeller pitch/diameter ratio	1.1
Propeller rake	4°3″
Propeller developed area/disk area ratio	0.688
Rudder span	600 mm
Rudder chord	180 mm
Rudder profiles	NACA 0020
Rudder distance from propeller disk	113.5

propeller axis, the X axis downstream-oriented along the tunnel centerline, the Y axis along the along the horizontal toward starboard, the Z axis along the upward vertical.

- A cylindrical reference frame O–XRθ with the origin O in the intersection between the propeller disk and the propeller axis, the X axis downstream-oriented along the propeller axis, the R axis along the radial outward, the azimuthal coordinate, θ, counter-clockwise positive.

3.2 Experimental configuration

In the present study, the propeller-rudder arrangement is the same used in Felli and Falchi (2011), and specifically, it was thought to simulate the typical configuration of a single-screw ship model. Specifically, the rudder was fixed with the symmetry plane passing through the prolongation of the propeller axis and the leading edge at $r = R$ from the propeller disk plane. A sketch of the experimental configuration is given in Fig. 3.

Rudder geometry was simulated using an all-movable-2D-wing having a rectangular planform and standard symmetrical sections with NACA0020 profiles. Propeller was the INSEAN E779A (see e.g., Cenedese et al. 1988; Calcagno et al. 2005; Felli et al. 2006).

Overall details of the propeller and rudder geometries are summarized in Table 1.

3.3 Pressure measurements

The detailed mapping of the wall pressure fluctuations over the rudder surface required the manufacturing of a special steel rudder such to flush mount a large number of sensors, to allow an adequate resolution and to avoid any possible water penetration into the circuit.

The adopted rudder consisted of a steel structure and two sets of three covers (i.e., one set per side) which were suitably designed to arrange different grid configurations at both sides of the rudder. More specifically, each cover was designed to host a maximum of 24 sensors simultaneously in four blocks with six positions each. The three covers had the same grid design, 0.1R and 0.2R shifted each other in the vertical direction. This allowed to map a total of 72 positions per side and, thus, to improve the spatial resolution of the measurement, constrained by sensor encumbrance otherwise.

The resulting arrangement is documented in Fig. 4.

Relative pressure transducers by ENTRAN (i.e., EPN D11) were used to measure pressure fluctuations signals. The main features of the pressure transducers are reported in Table 2.

Signals were acquired by the PROSIG P8200 acquisition system, setting the sampling rate at 40 kHz and the acquisition time at 100 s. Simultaneously, an once-per-revolution TTL trigger signal was acquired to synchronize pressure signals with the angular position of the propeller reference blade. The synchronization was carried out

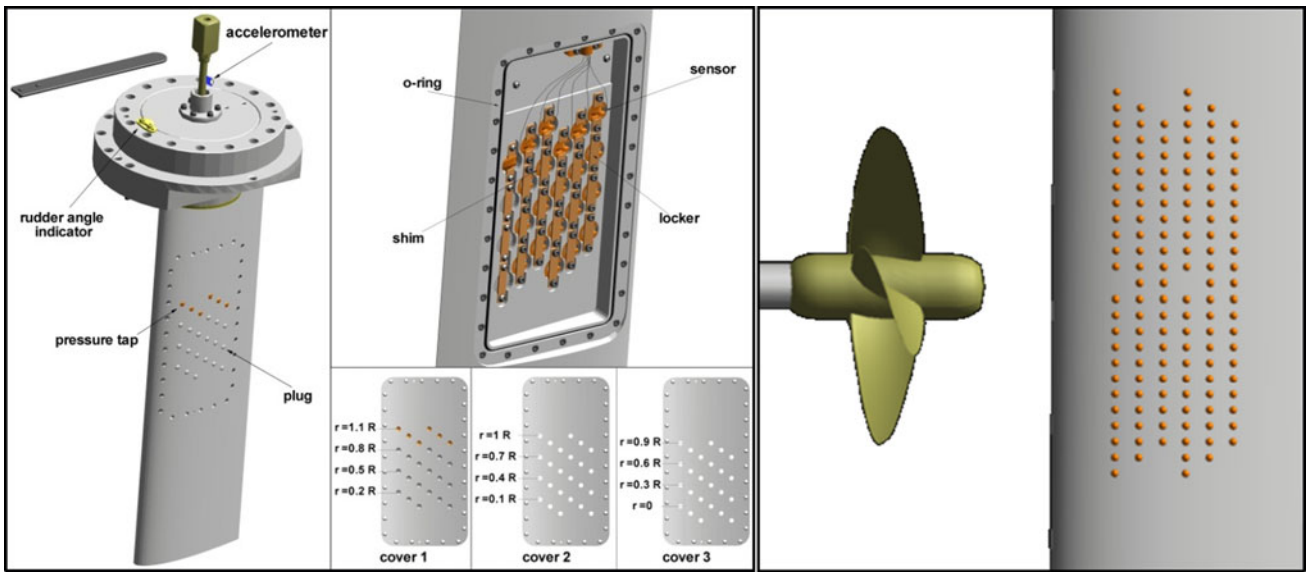

Fig. 4 Sketch of the instrumented rudder for the wall pressure measurements

Table 2 Main features of the pressure transducers

Full range	25 psi
Resonant frequency	15 kHz
Sensitivity	14 mV/psi

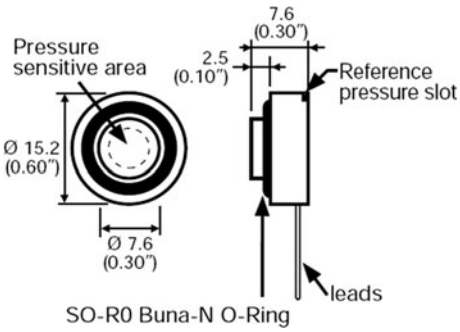

during data processing on the base of the pressure signal and the propeller TTL time histories. Then, pressure signals were phase averaged, using a slotting technique with 360 angular intervals in which pressure samples were arranged depending on the phase delay from the last trigger signal (Felli et al. 2006).

Considering the apparatus and the operational procedure, experimental and bias errors in the wall pressure measurements were estimated to be within 6 %. More specifically, the major contribution was represented by the perturbation induced by rudder vibrations, whose amplitude was as small as to give a contribution to the final uncertainty estimated within 5 %. The uncertainty in the statistical analysis, estimated using the *t*-Student distribution with 97.5 % confidence level, ranged from 0.1 to 0.5 % depending on the local standard deviation of pressure fluctuations. A calibration procedure in which sensors were subjected to a fluctuating acoustic pressure source of known amplitude was applied to measure the actual sensitivity of pressure transducers. Calibration showed variations in the sensitivity values as small as 0.2 %.

3.4 Experimental configuration

Tests were executed at the facility speed of $U_\infty = 5$ m/s. The propeller revolution speed was set to $n = 25$ rps. The corresponding value of the advance ratio $J = U_\infty/(\text{nD})$ was 0.88. Based on the rudder chord and the free-stream velocity, the nominal Reynolds number $\text{Re} = (U_\infty \bullet c)/v$ was around $\text{Re} = 1.36 \times 10^6$. This value increases of about 20 % if one accounts for the velocity acceleration induced by the propeller.

The test matrix includes:

- wall pressure measurements performed on a grid of 144 positions for 9 rudder deflections (i.e., from $-15°$ to $+15°$, 5° spaced).

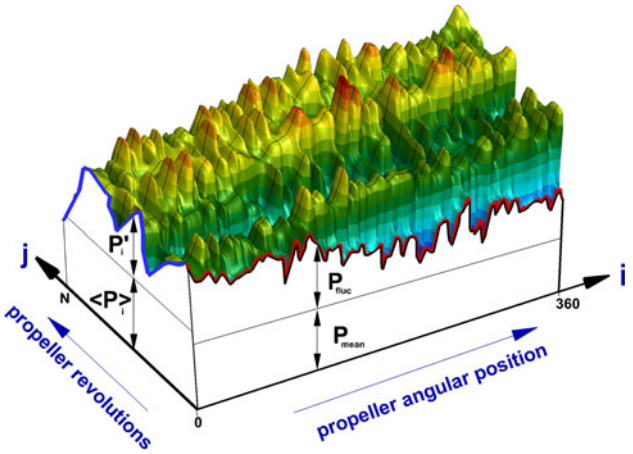

Fig. 5 Representation of the measured pressure signals

- Comparison of the phase-locked hydrodynamic and acoustic pressure distribution over the rudder surface with the corresponding vorticity field measured in a previous test campaign by Felli and Falchi (2011) at the same operating conditions. This comparison is limited to the deflection angle $\alpha = 0°$, this being the only rudder configuration at which velocity measurements were undertaken.

4 Result analysis

4.1 Pressure maps on rudder surfaces

The analysis of pressure distribution over the rudder surface is an effective tool for the identification of major perturbation sources related to the interaction between the propeller wake and the rudder. Maps were obtained interpolating the wall pressure signals over the measurement domain, after having processed them by the tools described Sects. 2.1 and 2.2. In particular, this procedure was applied to the acoustic and hydrodynamic parts of pressure signals, treated as separate signals according to decomposition technique described in Sect. 2.1. The analytical representation of the measured pressure signals, to which we will refer therein, is given below (Fig. 5):

$$P(x,y,z,\alpha,t) = P_{\text{mean}}(x,y,z,\alpha) + P_{\text{fluc}}(x,y,z,\alpha,t) \qquad (5)$$

where $P(x,y,z,\alpha,t)$ is the relative pressure signal acquired by a given transducer at the position x,y,z and at rudder deflection α, $P_{\text{mean}}(x,y,z,\alpha) = \frac{1}{T}\int_0^T P(x,y,z,\alpha,t)\mathrm{d}t$ represents the contribution of the static pressure plus the mean part of the dynamic pressure over the acquisition time T and $P_{\text{fluc}}(x,y,z,\alpha,t)$ is the fluctuating part of the dynamic pressure.

The phase-locked representation of the two terms on the right-hand side of Eq. (5) is:

$$P_i(x,y,z,\alpha,j) = \langle P_i(x,y,z,\alpha)\rangle + P'_i(x,y,z,\alpha,j) \qquad (6)$$

$$P_{\text{fluc}_i}(x,y,z,\alpha,j) = \langle P_{\text{fluc}_i}(x,y,z,\alpha)\rangle + P'_{\text{fluc}_i}(x,y,z,\alpha,j,\vartheta) \qquad (7)$$

where $i = 0\ldots0.359$ identifies the angular position of the propeller; $<P_i>$ is the phase-locked mean component of the relative pressure at the propeller position $\theta = i°$, calculated over N revolutions and P'_i is its fluctuating component; $\langle P_{\text{fluc}_i}\rangle = \frac{1}{N}\sum_{j=1}^{N} P_{\text{fluct}}(x,y,z,\alpha,i+j\cdot N)$ is the phase-locked mean component of the fluctuating part of the dynamic pressure at the propeller position $\theta = i°$, calculated over N revolutions and P'_{fluc_i} is its fluctuating component;

All the terms of Eqs. (5), (6) and (7) are reported in Fig. 6. For the sake of conciseness, contour plots of Fig. 6 describe only the results relative to the propeller position $\theta = 0°$.

Propeller unsteady perturbation appears completely embedded in the average contribution of the relative pressure as emerges by: (1) the substantial correspondence of the time-averaged and the phase-locked components of the relative pressure at any angular position of the propeller and (2) the about one order of magnitude less intense value of the fluctuating term compared to the steady one (see first column of Fig. 6).

In the present paper, focus will be mainly put on the analysis of the fluctuating contributions considering that noise and vibrations are correlated with unsteady events.

Result analysis is organized as follows. Phase-locked velocity and pressure maps are analyszd in Sect. 4.1.1. This analysis aims at the identification/characterization of the fundamental mechanisms of the hydrodynamic and acoustic perturbation on the rudder, and it is based on the comparison between phase-locked velocity and pressure distributions at the same propeller position. In Sect. 4.1.2, the effect of rudder deflection is dealt with through the analysis of the overall pressure signal and its fluctuating part.

Contour plots and comments in Sects. 4.1.1 and 4.1.2 refer to the rudder starboard and port upper regions relative to the propeller axis. However, it is worth noting that all the considerations made for a given deflection angle can be extended to the corresponding mirrored regions on lower part of the rudder for the opposite deflection, in view of both the on-average axisymmetric flow distribution of the propeller wake and the rudder position.

For the sake of conciseness, only the most representative results are reported hereinafter.

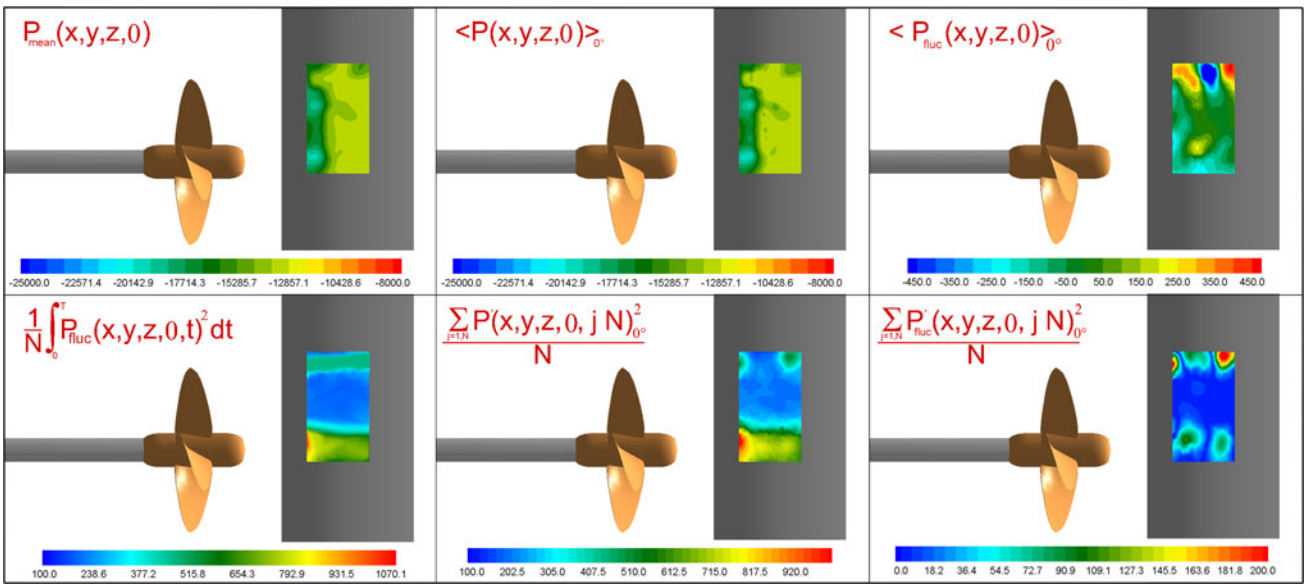

Fig. 6 Representation of the terms of Eqs. (5), (6) and (7) for the propeller-rudder configuration. Plots in second and third columns are relative to the propeller position $\theta = 0°$. *Top* mean components. *Bottom* RMS of the fluctuating components

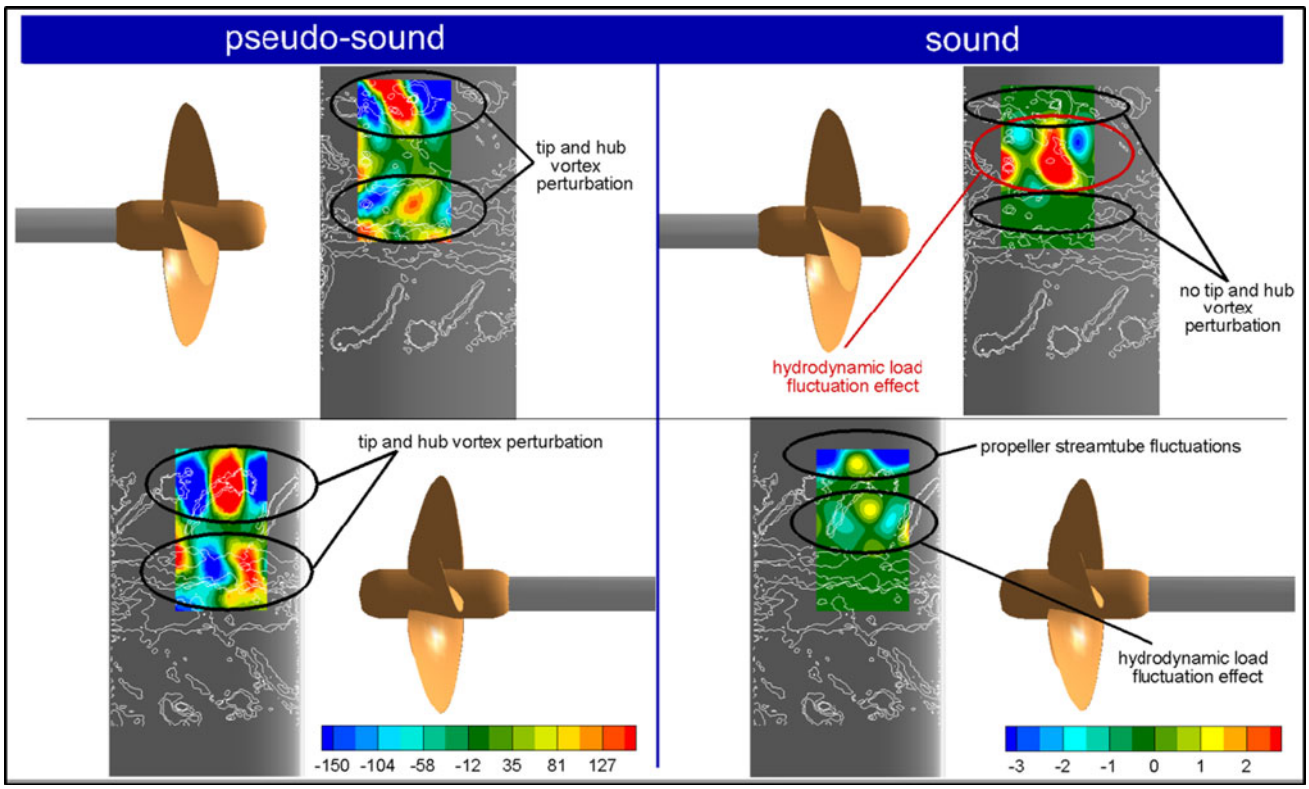

Fig. 7 Phase-locked comparison between the sound and pseudo-sound components of the wall pressure signal (*contour plots*) and the vorticity field measured over the rudder surface (*white lines*). *Top* port face. *Bottom* starboard face

4.1.1 *Comparison between velocity and pressure distributions*

Figure 7 reports the distribution of the phase-locked acoustic and hydrodynamic signals over the rudder surfaces for the deflection angle $\alpha = 0°$ (i.e., $\langle P_i(x,y,z,\alpha)\rangle_{sound}$ and $\langle P_i(x,y,z,\alpha)\rangle_{pseudo}$, respectively). The phase-locked evolution of the acoustic and hydrodynamic signals is documented in Fig. 8. The corresponding signature of the phase-locked vorticity

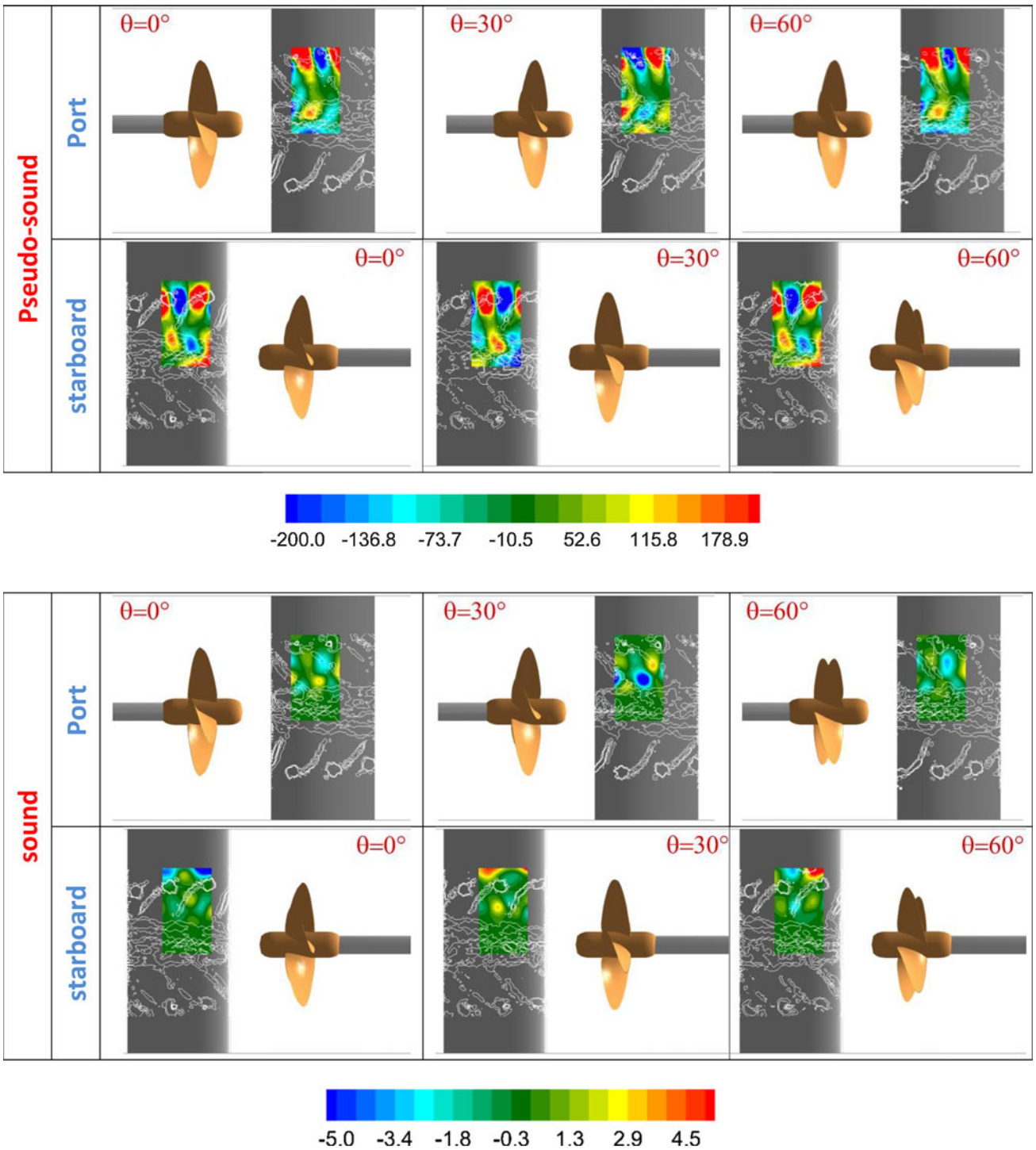

Fig. 8 Comparison between the sound and pseudo-sound components of the wall pressure signal (*contour plot*) and the vorticity field measured along the rudder surface (*white lines*). Pictures describe the phase-locked evolution at the propeller angular positions $\theta = 0°$, 30° and 60°

component $\omega_y(x, y, z, \theta)$ is represented by the superimposed white lines. Vorticity data are derived from previous velocity measurements by LDV performed at the same conditions and thoroughly documented in Felli and Falchi (2011).

Sound and pseudo-sound contributions exhibit different topologies which are evidently indicative of distinct mechanisms behind the acoustic and hydrodynamic perturbation in a propeller-rudder system.

Hydrodynamic perturbation is mainly localized in regions where propeller tip and hub vortices interact with the rudder and moves following their trace (see Figs. 7, 8). The occurrence of the largest hydrodynamic pressure

fluctuations in correspondence with the propeller tip and hub vortices (left of Figs. 7, 8) is indicative of their dominant contribution to both rudder vibrations and structural stresses. The trace of the tip vortex-associated perturbation has a dipolar pattern centered in the vortex core. A similar pattern has been shown in Ianniello et al. (2013) for the pressure field around a propeller tip vortex. The hydrodynamic pressure perturbation reduces dramatically moving inward along the trace of the trailing wake and, then, increases suddenly in the hub vortex region, where it presents again a dipolar pattern with inverted sign relatively to the corresponding tip sections. In both hub and tip regions, the sign of the dipole keeps constant during the propeller revolution. We hypnotize that this might be due to the counter rotating nature of the blade tip and root vortices that might induce a push–pull perturbation on the associated pressure fields.

Local maxima of the acoustic pressure $\langle P_i(x,y,z,\alpha)\rangle_{\text{sound}}$ are localized in the rudder region between the hub and the tip vortices, where propeller-induced hydrodynamic loads are maxima (see Felli et al. 2009), and radially outside the tip vortex trace, in correspondence with the boundary of the propeller streamtube. On the contrary, it seems that there is no evidence of a significant acoustic perturbation associated with the passage of the propeller structures (right of Fig. 7).

Therefore, the primary sources of tone sound in a propeller-rudder system seem to be basically correlated with two distinct phenomena: the hydrodynamic load unsteadiness induced by propeller flow, on the one hand, and the fluctuations of the propeller streamtube during the interaction with the rudder, on the other hand. The inward deflection of the propeller streamtube in the suction-side regions of the rudder, already highlighted in Felli and Falchi (2011), makes the latter perturbation visible only in the contour plots of the starboard side where the streamtube boundary falls inside the measurement region. On the contrary, boundary region of the propeller streamtube is external to the measurement grid on the port upper region of the rudder, and thus, there is no evidence of the associated pressure perturbation.

Unlike observed in the evolution of the hydrodynamic perturbation, acoustic pressure fluctuations are well localized and have a pulsating-like nature (Fig. 8).

4.1.2 *Effect of rudder deflection*

Propeller wake perturbation makes non-symmetrical pressure distribution over the starboard and port faces of the rudder when it is deflected of the same angle in the clockwise and counter-clockwise direction. This effect is the obvious consequence of Eq. (1), which describes the rudder spanwise distribution of the hydrodynamic incidence $\beta(s)$:

$$\beta(s) = \alpha - a\tan\left(\frac{V(s,\theta)}{U(s,\theta)}\right) \tag{8}$$

where s is the curvilinear abscissa along the rudder span, α is the deflection angle, $U(s)$ and $V(s)$ are the axial and transversal components of the velocity upstream of the leading edge (Fig. 9).

In particular, with reference to the case of a right-handed propeller, the direction of the transversal velocity is such to increase (reduce) the effective incidence of the rudder for positive (negative) deflections, in the propeller rotation upper part of the rudder. The opposite trend characterizes the lower part of the appendage according to the skew-symmetrical distribution of the propeller perturbation along the span.

The distribution of the phase-locked mean pressure relative to the propeller position $\theta = 0°$ $\langle P(x,y,z,\alpha)\rangle_0$ versus the deflection angle of the rudder is documented in Fig. 10 (the same comments are valid for the time-averaged pressure distribution $P_{\text{mean}}(x,y,z,\alpha)$, as described in Sect. 4.1).

Contour plots and comments refer to the rudder starboard and port upper regions relative to the propeller axis.

The contribution at the blade harmonic $\langle P_{\text{fluc}_0}(x,y,z,0)\rangle_{\text{blade}}$ is dominant within the whole range of analyzed deflections. As a matter of fact, the topologies of the pressure fluctuation signals $\langle P_{\text{fluc}_0}(x,y,z,0)\rangle$ at $\alpha = 0$ (Fig. 7) trace quite accurately those obtained considering only the contribution at the blade harmonic $\langle P_{\text{fluc}_0}(x,y,z,0)\rangle_{\text{blade}}$(Fig. 12), both for the acoustic and the hydrodynamic parts.

The blade harmonic contribution to the acoustic pressure fluctuations is significantly larger on the high-pressure face of the rudder (i.e., starboard and port faces in the rudder upper region for positive and negative deflections, respectively) and tends to rise when the deflection angle is increased. In particular, the acoustic signal shows an abrupt intensification in correspondence with the rudder deflection $\alpha = 15°$.

At $\alpha = 0°$ deflection, the non-symmetrical distribution of the wall pressure on the rudder surfaces is exclusively due to the propeller perturbation, which is such to reduce (increase) pressure on the starboard (port) face of the rudder upper region. Pressure unbalance between the starboard and port surfaces of the rudder tends to even out, on average, around $\alpha = 5°$, which thus represents the deflection at which propeller effect is about compensated by the geometrical incidence. Starting from the "neutral" deflection and increasing further the rudder angle in the counter-clockwise direction, the low pressure region moves definitely to the port of the rudder and the pressure difference.

Between the face and back surfaces tends to increase more and more, albeit it keeps significantly less than at corresponding clockwise deflections.

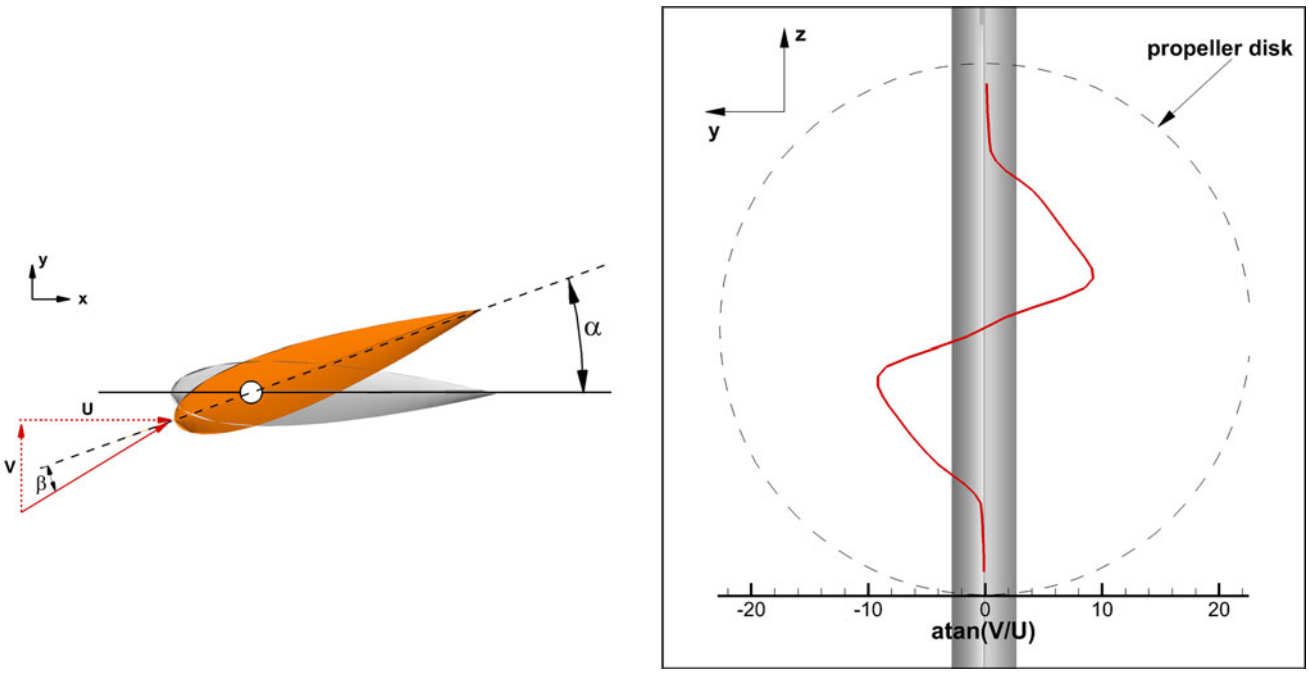

Fig. 9 Measurement grid for the LDV measurements on the rudder surface

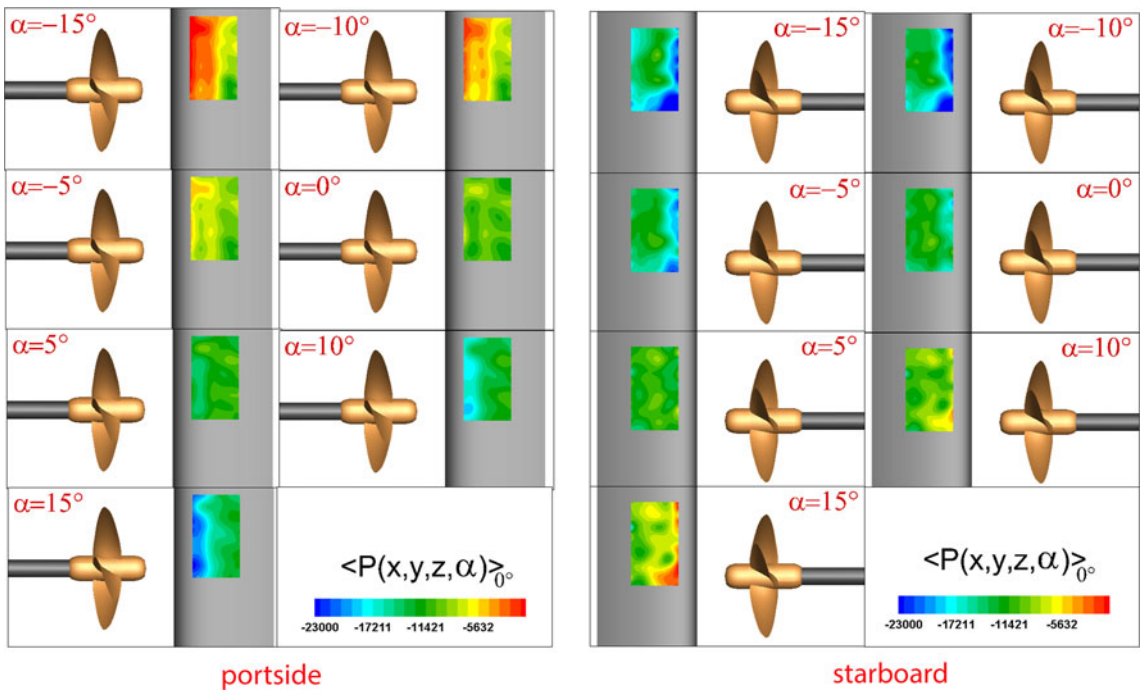

Fig. 10 Phase-locked mean pressure relative to the propeller position $\theta = 0°$ ($< P(x, y, z, \alpha) >_0$) at different deflection angles of the rudder

It follows that the critical incidence, nominally around 20° for a NACA 0020 profile at $Re = 10^6$, increases (reduces) for counter-clockwise (clockwise) deflections in the upper region of the rudder.

Figures 11 and 12 describe the effect of rudder deflection on the topologies of the acoustic and hydrodynamic pressure fluctuations $\left\langle P_{\mathrm{fluc}_{0°}}(x, y, z, \alpha) \right\rangle$, relative to the propeller position $\theta = 0°$.

On the suction side, acoustic energy is observed to have a maximum at about 25–30 % of the rudder chord in the region where rudder experiences the larger

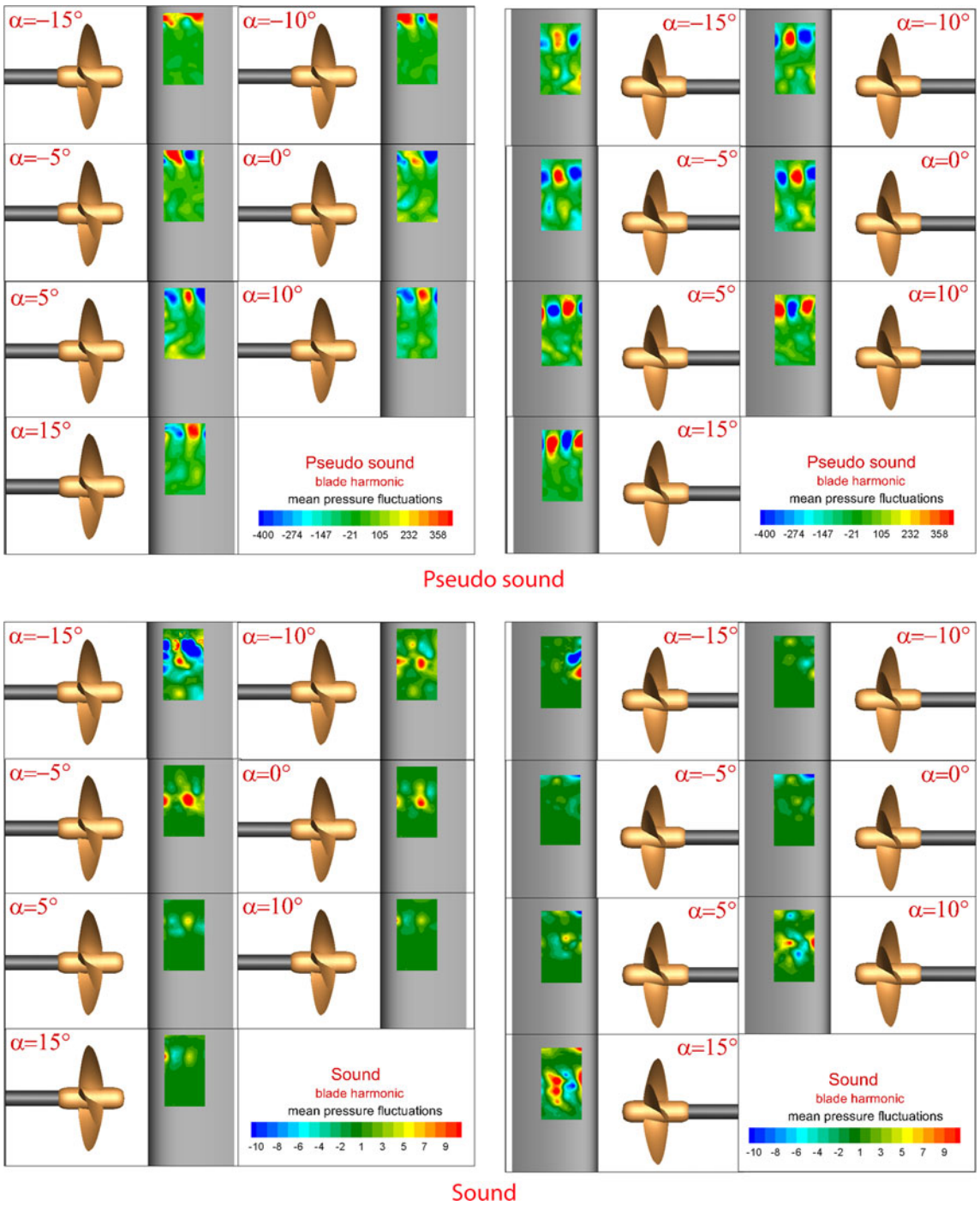

Fig. 11 Phase-locked snapshot of the sound (*bottom*) and pseudo-sound (*top*) pressure fluctuations at different rudder deflections: blade harmonic contribution

hydrodynamic load fluctuations, i.e., around 0.7R outward the rotation axis. The intensity of such a maximum tends to increase with the deflection angle (i.e., negative deflections starboard and positive deflection port), and at a given deflection, it is larger on the starboard side of the rudder because of the larger hydrodynamic incidence (see Eq. 8). We hypnotize that this behavior might be explained considering the typical pressure distribution over the suction side of a wing and specifically the fact that:

1. the suction peak of a wing is located at about 25–30 % of the chord which corresponds to the region where acoustic energy has a maximum, approximately;

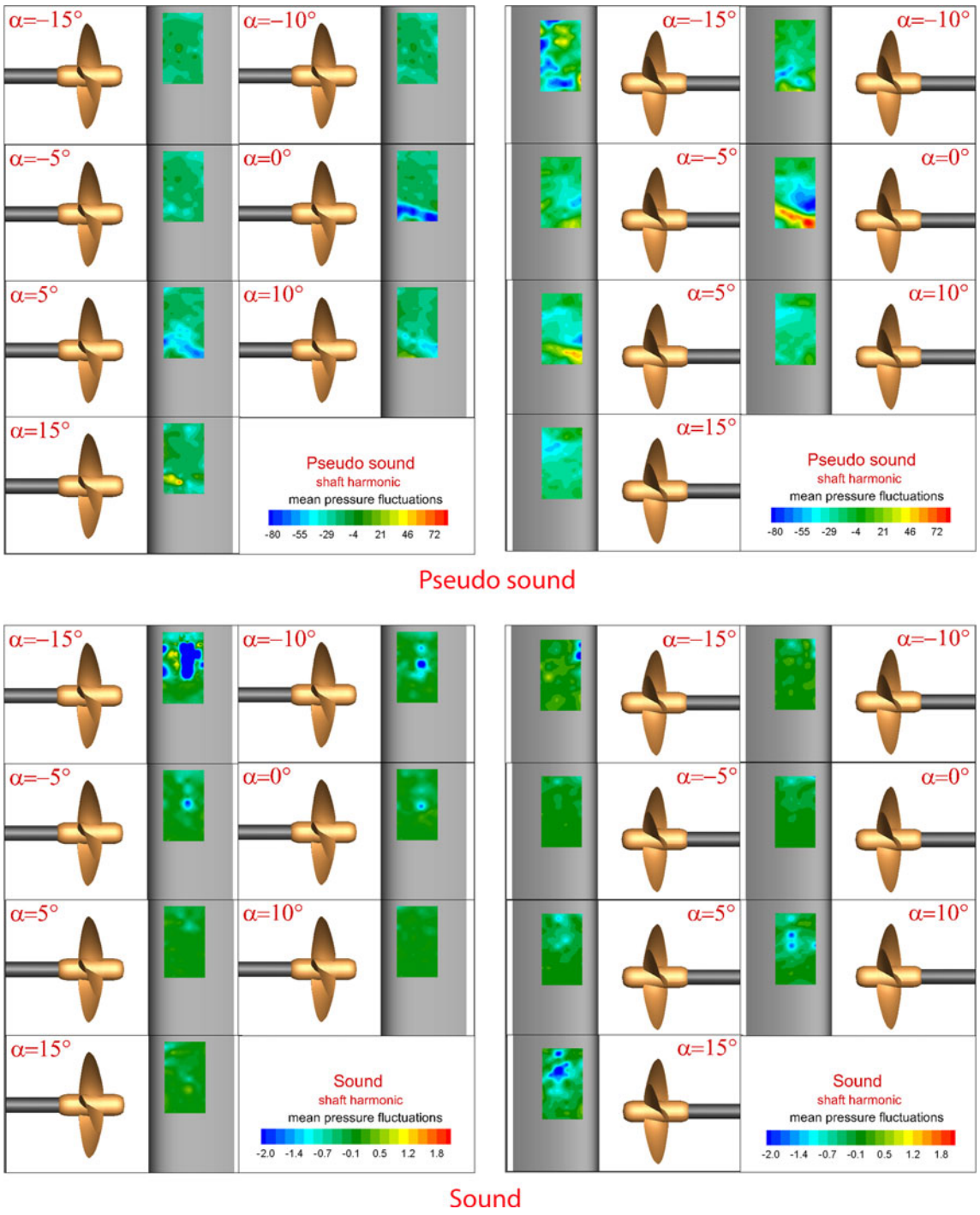

Fig. 12 Phase-locked snapshot of the sound (*bottom*) and pseudo-sound (*top*) pressure fluctuations at different rudder deflections: shaft harmonic contribution

2. the intensity and the slope of the suction peak rise rapidly when the angle of attack is increased. Furthermore, for a given oscillation range of the hydrodynamic load, intensity and slope variations of the suction peak tend to get larger and larger when angle of attack is increased.

The shaft harmonic contribution to hydrodynamic pressure fluctuations $\langle P_{\mathrm{fluc}_0}(x,y,z,0)\rangle_{\mathrm{shaft}}$ is dominated by the effect of the hub vortex, as clearly emerges by the occurrence of the maximum fluctuation values in the region $-0.4\mathrm{R} \leq \mathrm{z} \leq 0.4\mathrm{R}$.

The hub vortex perturbation affects both the starboard and the port faces of rudder when the deflection angle is within the range 0°–5° and appears as a push–pull perturbation on the associated pressure fields. For example, the

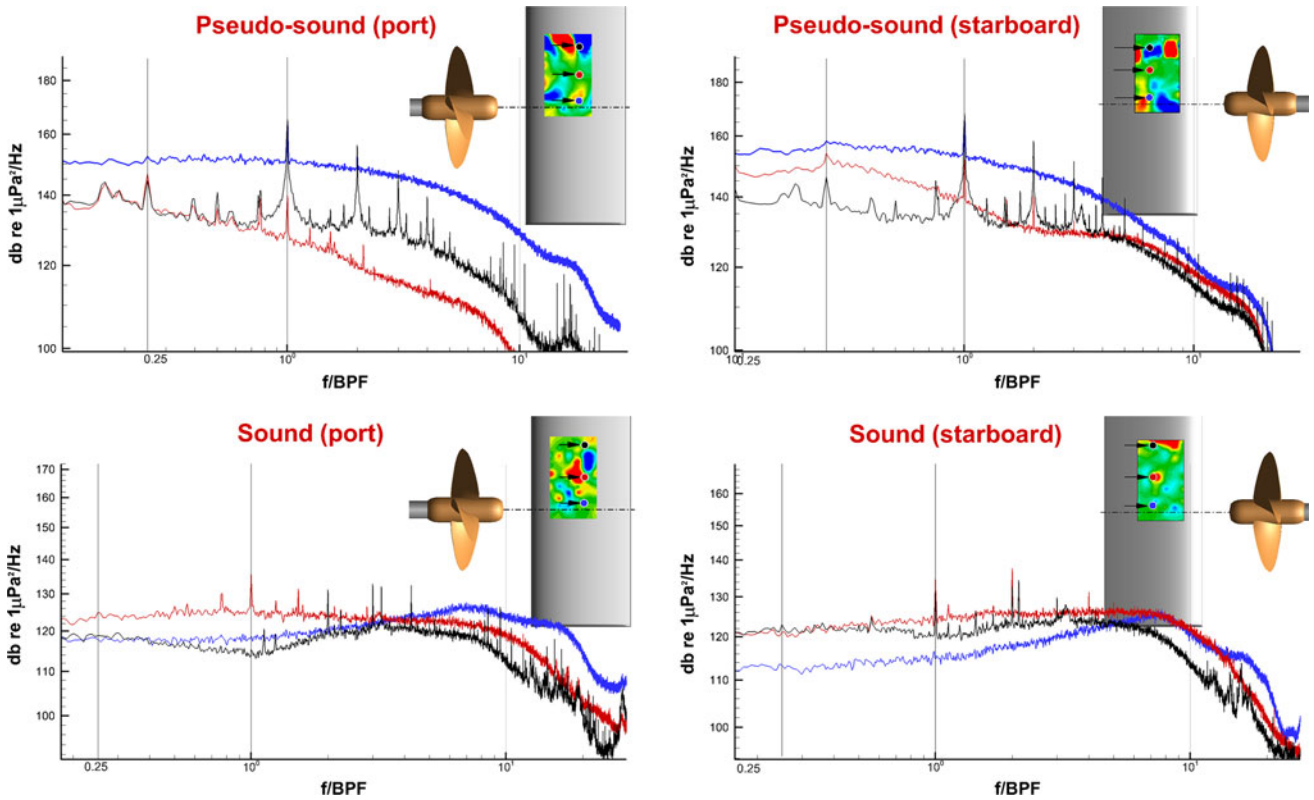

Fig. 13 Power spectral density of the acoustic and hydrodynamic sound pressure fluctuations in some representative positions on the rudder surface (main frame). Phase-locked topologies of the wall pressure distribution over the rudder surface (frame at the *top-right-hand side*)

sign of $\langle P_{\mathrm{fluc}_0}(x,y,z,0)\rangle_{\mathrm{shaft}}$, positive on the starboard face and negative on the pressure face at $\alpha = 0°$, reverses at $\alpha = 5°$ (Fig. 12). At larger deflections, the signature of the hub vortex perturbation exhibits a significant decay and interests only one side of the rudder. This behavior, also visible in the plots at the blade harmonics in Fig. 11, is due to the fact that rudder position has a zero offset relative to the propeller axis: when the deflection angle exceeds about 5° in magnitude the hub vortex tends to be deflected toward port for positive deflections or starboard side for negative deflections.

Acoustic pressure fluctuations at the shaft harmonic keep about negligible within the range of rudder deflections from $-10°$ to 10°. At the larger deflection angles (i.e., $|\alpha| > 10°$), acoustic perturbation manifests a sudden increase on the pressure side (Fig. 12).

4.2 Spectral characteristics of acoustic and hydrodynamic pressure fluctuations over the rudder surface

Figure 13 shows the power spectral density of the sound and pseudo-sound pressure fluctuations in some representative positions along the rudder surface. The corresponding phase-locked topologies based on pressure fluctuation signals $\langle P_{\mathrm{fluc}_i}(x,y,z,\alpha)\rangle$ are reported on the top-right-hand side of each figure by contour plots.

The analyzed positions were selected according to the results of Sect. 4.1 in correspondence with the local maxima of the acoustic and hydrodynamic pressure fluctuation signals. In particular, these positions belong to three zones, namely "zone 1," "zone 2" and "zone 3," which are located in correspondence with the top (i.e., $0.85 < z/R < 1.1$), middle (i.e., $0.4 < z/R < 0.8$) and bottom (i.e., $0 < z/R < 0.3$) regions of the propeller rotation upper part of the rudder, respectively.

At large, pressure spectra over the rudder surface exhibit a broadband component and a series of harmonically related tonal peaks, mostly at multiples of the blade passing frequency (BPF) and more or less acute depending on both position and perturbation type (i.e., acoustic or hydrodynamic).

More specifically, the following results can be drawn by the analysis of Fig. 13:

- The hydrodynamic and acoustic spectra show different trends and intensities in the broadband component. In particular, hydrodynamic spectra have a constant intensity in the low frequency range (i.e., f/BPF < 1

in zones 1 and 3 and f/BPF < 0.25 in zone 2) and, then, decay about monotonically conforming with the $-11/3$ power law. On the contrary, trends of the acoustic counterparts change dependently on the spanwise position along the rudder, at least for the frequency band f/BPF < 8. Specifically, broadband spectra for zone 1 decay with a minimum at the blade passing frequency, increase slightly in the frequency band $1 <$ f/BPF < 6 and, then, decay definitely according to $-15/3$ power law. In zone 2, broadband spectra keep constant over the low frequency range and, then, decay with a $-15/3$ power law. Finally, zone 3 presents an on-average constant trend in the frequency band $1 <$ f/BPF < 6, followed by an increase and a rapid decay of the broadband spectrum which returns a hump with the maximum at about f/BPF $= 8$.

- The broadband part of the hydrodynamic perturbation dominates the low frequency bands where it is about 25–30 dB re 1 μPa 2/Hz larger than the acoustic counterpart. The opposite behavior is observed in the mid-frequency range (i.e., $0.2 <$ f/BPF < 2), instead. Frequencies at which the power spectra of the acoustic and hydrodynamic signals intersect to each other correspond to about f/BPF $=$ 8–9 in zones 1 and 3, and f/BPF $= 2.5$ and 5 in the port and starboard sides of zone 2, respectively.
- The overall broadband spectra of the hydrodynamic signals in zones 3 are about 5 and 12 dB re 1 μPa 2/Hz larger than elsewhere. This behavior is likely to be the consequence of the local turbulence content in the hub vortex region which is much larger compared to those in the propeller tip vortex and in mid-blade span regions of the rudder (Felli and Falchi 2011).
- Tonal peaks of acoustic and hydrodynamic spectra are mostly related to harmonics and sub-harmonics of the blade passing frequency. In particular, the peak at the blade harmonic is the fundamental frequency of the hydrodynamic spectrum in zones 1 and 2 and of the acoustic counterpart in zone 3. This peak reduces significantly or disappears elsewhere (i.e., zone 3 in the acoustic spectra, zones 1 and 2 in the hydrodynamic spectra, respectively), where other harmonics dominate the spectrum. These results, confirmed by the contour plot representation in Fig. 7, are clearly indicative of distinct mechanisms behind the acoustic and hydrodynamic perturbation in a propeller-rudder system. We delved into this point in Sect. 4.1.
- The relative intensity of the tonal and broadband contributions shows a clear dependency on both frequency, perturbation type (i.e., acoustic and hydrodynamic) and position (i.e., zone 1, zone 2 and zone 3). In particular, tonal noise peaks emerge from the acoustic spectra of about 10 dB re 1 μPa 2/Hz at most in zones 1 and 2 and disappear in zone 3, where signals present a totally broadband energy distribution. Conversely, tonal peaks are much more prominent in the power spectra of the hydrodynamic signals, especially in zones 1 and 3. Moreover, unlike the hydrodynamic spectra, which present a quite rich harmonic content, tonal noise peaks of the acoustic perturbation concern only few harmonics and inter-harmonics of the blade passage frequency. From this result, it is possible to conclude that the overall hydrodynamic perturbation on the rudder is mainly due to periodic events correlated with the dynamics of the propeller tip and hub vortices. On the other hand, the relatively stronger broadband contribution in the acoustic spectra suggests that random events such as those related to turbulence ingestion from the propeller wake have a relevant influence on the overall signature. This result is supported by the numerous studies dealing with the effect of turbulent ingestion on the broadband noise (see e.g., Paterson and Amiet 1976).

5 Conclusions and future works

Nowadays, the identification of the noise and vibration sources in marine propulsion is a topical subject to deal with, due to the increasing restrictions on environmental noise levels and also because of the consumer's demands. In response to this challenge, the present study introduces a novel approach for the identification and analysis of the hydrodynamic and hydroacoustic mechanisms of perturbation in a naval unit. The approach consists of near-field velocity and pressure phase-locked measurements and advanced post-processing techniques by which separating out the acoustic from the hydrodynamic components of the pressure fluctuation signals. Subject of the study was the analysis of the noise and vibration sources in a rudder operating behind a marine propeller. The investigation concerned near-field pressure fluctuations measurements on the starboard and port surfaces of the rudder. Spectral content and topologies of the sound- and pseudo-sound-related pressure fluctuations were characterized at different deflections angles, emphasizing the fundamental phenomena that govern the acoustic and hydrodynamic perturbation on the rudder. In particular, the study highlighted distinct mechanisms underlying the acoustic and hydrodynamic pressure fluctuations on the rudder. On the one hand, structural stresses and induced vibrations on the rudder are mainly influenced by the perturbation of the propeller tip and hub vortices, whose contributions dominate the hydrodynamic part of pressure fluctuations. On the other hand, the acoustic field is basically generated by both

deterministic and random variations in rudder loading and shear layer fluctuations of the propeller streamtube. Instead, differently from the hydrodynamic perturbation, tip and hub vortex passage does not cause any appreciable effect to acoustic field.

In spite of the light shed on the properties of the hydrodynamic and acoustic perturbations, a number of open issues still concern the hydroacoustics of a propeller-rudder system. Among the others, these include the mechanisms of noise propagation, the acoustic efficiency of the noise sources and the effect of cavitation. To this purpose, as a future development, we believe it will be quite valuable to extend our analysis to cavitating propeller-rudder configurations and to use spatially extended hydrophone arrays and conditional techniques to address the noise propagation aspects.

Acknowledgments This work was partially supported by the Italian Ministry of Defence in the framework of the research project "PRIAMO" and partially by the Italian Ministry of Education, University and Research in the framework of the research project "RITMARE", coordinated by CNR.

References

Anschau P, Mach KP (2009) Stereoscopic PIV measurements of rudder flow and vortex systems in the towing task. ATM 09, Nantes, France

Arndt RE, Long DF, Glauser MN (1997) The proper orthogonal decomposition of pressure fluctuations surrounding a turbulent jet. J Fluid Mech 340:1–33

Biot M, De Lorenzo F (2008) Some notes on the sound reduction index of pax cabins panels on cruise ships. J Acoust Soc Am 123(5):1101–1106

Calcagno G, Di Felice F, Felli M, Pereira F (2005) A stereo-PIV investigation of a propeller's wake behind a ship model in a large free-surface tunnel. Mar Technol Soc J 39(2):94–102

Carlton JS, Vlasic D (2005) Ship vibration and noise: some topical aspects. 1st international ship noise and vibration conference, London, UK

Cenedese A, Accardo L, Milone R (1988) Phase sampling in the analysis of a propeller wake. Exp Fluids 6:55–60

Chainais P, Abry P, Pinton JF (1999) Intermittency and coherent structures in a swirling flow: a wavelet analysis of joint pressure and velocity measurements. Phys Fluids 2(11):3524–3539

Daubechies I (1992) Ten lectures on wavelets. CBMS-NSF regional conference series in applied mathematics. Society for Industrial and Applied Mathematics. ISBN 978-0898712742

Farge M (1992) Wavelet transforms and their applications to turbulence. Ann Rev Fluid Mech 24:395–457

Farge M, Schneider K, Kevlahan N (1999) Non-Gaussianity and coherent vortex simulation for two-dimensional turbulence using an adaptive orthogonal wavelet basis. Phys Fluids 11:2187–2201

Felli M, Di Felice F (2004) Analysis of the propeller-hull interaction by LDV phase sampling techniques. J Vis 7:77–84

Felli M, Falchi M (2011) Propeller tip and hub vortex dynamics in the interaction with a rudder. Exp Fluids 51(5):1385–1402

Felli M, Di Felice F, Guj G, Camussi R (2006) Analysis of the propeller wake evolution by pressure and velocity phase measurements. Exp Fluids 41:441–451

Felli M, Camussi R, Guj G (2009) Experimental analysis of the flow field around a propeller-rudder configuration. Exp Fluids 46: 147–164

Ffowcs-Williams J (1992) Noise source mechanisms. In: Modern Methods in Analytical Acoustics Lecture Notes. Springer, Berlin, pp 313–354

Grizzi S, Camussi R (2012) Wavelet analysis of near-field pressure fluctuations generated by a subsonic jet. J Fluid Mech 544: 277–307

Guitton A, Jordan P, Laurendeau E, Delville J (2007) Velocity dependence of the near pressure field of subsonic jets: understanding the associated source mechanisms. AIAA Paper 2007-3661

Hildebrand J (2004) Sources of anthropogenic sound in the marine environment. Scripps Institution of Oceanography, University of California San Diego, USA, California

Howe WL (1960) Similarity of far noise fields of jets. NASA technical report, R-52

Ianniello S, Muscari R, Di Mascio A (2013) Ship underwater noise assessment by the acoustic analogy part II: hydroacoustic analysis of a ship scaled model. J Mar Sci Technol (in press)

Lücke T, Streckwall H (2009) Cavitation research on a very large semi spade rudder. First international symposium on marine propulsors, SMP'09, Trondheim, Norway

Mallat S (1989) A theory for multi resolution signal decomposition: the wavelet representation. Trans IEEE Pattern Anal Mach Intell 11:674–693

Paterson RW, Amiet RK (1976) Acoustic radiation and surface pressure characteristics of an airfoil due to incident turbulence. NASA CR-2733

Ribner HS (1964) The generation of sound by turbulent jets. Adv Appl Mech VIII:103–182

Ruppert-Felsot J, Farge M, Petitjeans P (2009) Wavelet tools to study intermittency: application to vortex bursting. J Fluid Mech 636:427–453

Tinney CE, Jordan P, Delville J, Hall AM, Glauser MN (2007) A time-resolved estimate of the turbulence and sound source mechanisms in a subsonic jet flow. J Turbul 8(7):1–20

Ukeiley LS, Ponton MK (2004) On the near field pressure of a transonic axisymmetric jet. Int J Aeroacoust 3(1):43–66